CrystEngComm c9ce00046a

We have presented the Graphical Abstract text and image for your article below. This brief summary of your work will appear in the contents pages of the issue in which your article appears.

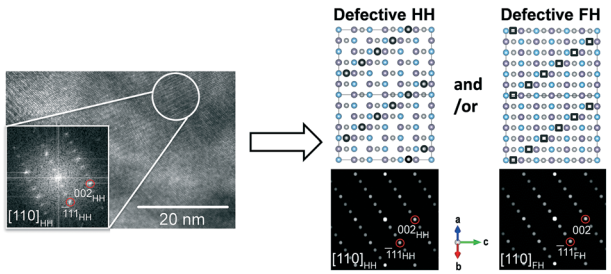

Long- and short-range structures of $Ti_{1-x}Hf_xNi_{1.0/1.1}Sn$ half-Heusler compounds and their electric transport properties

Matylda N. Guzik, Matthias Schrade, Raluca Tofan, Patricia A. Carvalho, Kristian Berland, Magnus H. Sørby, Clas Persson, Anette E. Gunnæs and Bjørn C. Hauback

Experimental study reveals the apparent ordered arrangement of excess Ni at the nominally vacant sublattice in thermoelectric $Ti_{1-x}Hf_xNi_{1.0/1.1}Sn$ half-Heusler compounds.

Please check this proof carefully. Our staff will not read it in detail after you have returned it.

Please send your corrections either as a copy of the proof PDF with electronic notes attached or as a list of corrections. **Do not edit the text within the PDF or send a revised manuscript** as we will not be able to apply your corrections. Corrections at this stage should be minor and not involve extensive changes.

Proof corrections must be returned as a single set of corrections, approved by all co-authors. No further corrections can be made after you have submitted your proof corrections as we will publish your article online as soon as possible after they are received.

Please ensure that:

- The spelling and format of all author names and affiliations are checked carefully. You can check how we have identified the authors' first and last names in the researcher information table on the next page. **Names will be indexed and cited as shown on the proof, so these must be correct.**
- Any funding bodies have been acknowledged appropriately and included both in the paper and in the funder information table on the next page.
- All of the editor's queries are answered.
- Any necessary attachments, such as updated images or ESI files, are provided.

Translation errors can occur during conversion to typesetting systems so you need to read the whole proof. In particular please check tables, equations, numerical data, figures and graphics, and references carefully.

Please return your **final** corrections, where possible within **48 hours** of receipt, by e-mail to: crystengcomm@rsc.org. If you require more time, please notify us by email.

Funding information

Providing accurate funding information will enable us to help you comply with your funders' reporting mandates. Clear acknowledgement of funder support is an important consideration in funding evaluation and can increase your chances of securing funding in the future.

We work closely with Crossref to make your research discoverable through the Funding Data search tool (http://search.crossref.org/funding). Funding Data provides a reliable way to track the impact of the work that funders support. Accurate funder information will also help us (i) identify articles that are mandated to be deposited in **PubMed Central (PMC)** and deposit these on your behalf, and (ii) identify articles funded as part of the **CHORUS** initiative and display the Accepted Manuscript on our web site after an embargo period of 12 months.

Further information can be found on our webpage (http://rsc.li/funding-info).

What we do with funding information

We have combined the information you gave us on submission with the information in your acknowledgements. This will help ensure the funding information is as complete as possible and matches funders listed in the Crossref Funder Registry.

If a funding organisation you included in your acknowledgements or on submission of your article is not currently listed in the registry it will not appear in the table on this page. We can only deposit data if funders are already listed in the Crossref Funder Registry, but we will pass all funding information on to Crossref so that additional funders can be included in future.

Please check your funding information

The table below contains the information we will share with Crossref so that your article can be found *via* the Funding Data search tool. **Please check that the funder names and grant numbers in the table are correct and indicate if any changes are necessary to the Acknowledgements text.**

Funder name	Funder's main country of origin	Funder ID (for RSC use only)	Award/grant number
Norges Forskningsråd	Norway	501100005416	THELMA/No. 228854

Researcher information

Please check that the researcher information in the table below is correct, including the spelling and formatting of all author names, and that the authors' first, middle and last names have been correctly identified. **Names will be indexed and cited as shown on the proof, so these must be correct.**

If any authors have ORCID or ResearcherID details that are not listed below, please provide these with your proof corrections. Please ensure that the ORCID and ResearcherID details listed below have been assigned to the correct author. Authors should have their own unique ORCID iD and should not use another researcher's, as errors will delay publication.

Please also update your account on our online manuscript submission system to add your ORCID details, which will then be automatically included in all future submissions. See here for step-by-step instructions and more information on author identifiers.

First (given) and middle name(s)	Last (family) name(s)	ResearcherID	ORCID
Matylda N.	Guzik		0000-0001-6349-4659
Matthias	Schrade		0000-0002-9501-6536
Raluca	Tofan		
Patricia A.	Carvalho		
Kristian	Berland		
Magnus H.	Sørby		

Clas	Persson		
Anette E.	Gunnæs		
Bjørn C.	Hauback		

Queries for the attention of the authors

Journal: **CrystEngComm**

Paper: **c9ce00046a**

Title: **Long- and short-range structures of $Ti_{1-x}Hf_xNi_{1.0/1.1}Sn$ half-Heusler compounds and their electric transport properties**

For your information: You can cite this article before you receive notification of the page numbers by using the following format: (authors), CrystEngComm, (year), DOI: 10.1039/c9ce00046a.

Editor's queries are marked on your proof like this Q1, Q2, etc. and for your convenience line numbers are indicated like this 5, 10, 15, ...

Please ensure that all queries are answered when returning your proof corrections so that publication of your article is not delayed.

Query Reference	Query	Remarks
Q1	Please confirm that the spelling and format of all author names is correct. Names will be indexed and cited as shown on the proof, so these must be correct. No late corrections can be made.	
Q2	Do you wish to indicate the corresponding author(s)? If so, please specify the corresponding author(s).	
Q3	Ref. 49: Please give the name of this journal in full, including any other names by which this journal may be known (e.g. Chin. J. Struct. Chem. is also known as Jiegou Huaxue), so that its CASSI abbreviation can be checked for indexing purposes.	

CrystEngComm

PAPER

Long- and short-range structures of $Ti_{1-x}Hf_xNi_{1.0/1.1}Sn$ half-Heusler compounds and their electric transport properties†

Cite this: DOI: 10.1039/c9ce00046a

Matylda N. Guzik, ‡[ab] Matthias Schrade, [b] Raluca Tofan,[b] Patricia A. Carvalho,[c] Kristian Berland,[bd] Magnus H. Sørby,[a] Clas Persson,[b] Anette E. Gunnæs[b] and Bjørn C. Hauback[a]

A commercially feasible, nontoxic material that would convert heat into electricity in an efficient and cheap way has not yet been identified. Half-Heusler compounds are one the most interesting candidates but to become competitive their thermoelectric properties still need to be improved. Atomic substitution and excess Ni in the crystal structure of ternary MNiSn half-Heuslers are among the most successful approaches used to boost their performance. Here, we report on the effect of both methods applied simultaneously to the series of polycrystalline $Ti_{1-x}Hf_xNi_{1.0/1.1}Sn$, x = 0.00, 0.10, 0.15, 0.20, samples. High-resolution synchrotron powder X-ray diffraction studies combined with transmission electron microscopy demonstrate the crystallization of single or multiple Hf-substituted half-Heusler phase(s). The analysis of their long-range atomic structures shows that most of them contain interstitial Ni atoms disorderly distributed at the nominally vacant 4d sites. However, the short-range atomic correlations suggest that, for some compositions, excess Ni creates an orderly arranged additional atomic plane at the vacant fcc sublattice, which can be seen as a defective half- and/or full-Heusler phase. The results also show that the Ni-rich samples crystallize with the micrometer-sized full-Heusler phases, while all Hf-incorporating compositions present dispersion of HfO_2 nanoprecipitates in the grains of the half-Heusler matrix. This research is complemented by thermoelectric transport measurements of the studied compositions in the range of 300–750 K. The results suggest that neither Seebeck coefficient nor electrical resistivity shows an obvious correlation with the observed microstructures. These finding are discussed with respect to previously proposed transport mechanisms.

Received 9th January 2019,
Accepted 4th May 2019

DOI: 10.1039/c9ce00046a

rsc.li/crystengcomm

Introduction

A good thermoelectric (TE) material is defined by high energy conversion efficiency, light weight, good chemical and mechanical stability, low-toxicity and an affordable price.[1] Half-Heusler (HH) compounds potentially satisfy all above conditions and for this reason have been extensively investigated over the last two decades.[2] These cost-effective materials, consisting of environmental friendly and abundant elements, are chemically stable in the medium to high temperature range (600–1100 K).[3–5] However, the HHs still present challenges that must be addressed before they can be effectively implemented in technological applications. One of the main obstacles is their high thermal conductivity as compared to current alternatives.[5,6] Thus, to enhance the TE performance of HHs, various synthesis and processing methods, modifying chemistry and microstructure (*e.g.* atomic substitution, doping, nanostructuring), have been applied separately or jointly.[4,5,7,8] Although, the advances achieved so far demonstrate that their TE properties can be significantly improved, our understanding of key factors that govern the TE efficiency of HHs is still limited. This is mostly due to the strong research focus on thermal and electric transport properties of this family of compounds and less attention to their structural characterization. In addition, there is large variation in the data reported for nominally identical HH compositions, prepared by either the same or different synthesis methods.

[a] *Physics Department, Institute for Energy Technology, P.O. Box 40, N-2027 Kjeller, Norway*
[b] *Department of Physics, Centre for Materials Science and Nanotechnology, University of Oslo, P.O. Box 1048 Blindern, N-0316 Oslo, Norway*
[c] *SINTEF Materials and Chemistry, P.O. Box 124 Blindern, N-0314 Oslo, Norway*
[d] *Faculty of Science and Technology, Norwegian University of Life Sciences, P.O. Box 5003 NMBU, N-1432 Ås, Norway*

† Electronic supplementary information (ESI) available: 1) Graphical representation of Rietveld refinement results for all studied compositions, 2) STEM images with formed phases/nanoprecipitates in the investigated materials, 3) plots of S and ρ *vs.* occupancy of the 4d site, abundance of FH and HfO_2 in studied samples. See DOI: 10.1039/c9ce00046a

‡ The main author is currently working at the Department of Technology Systems of the University of Oslo. E-mail: m.n.guzik@its.uio.no.

From this perspective, insight into the relationship between structural and TE properties of both already studied and yet unexplored HH compositions is needed to accelerate progress in the field.

N-type HHs, with the general chemical formula **ABC** (**A**, **B**-transition metal atom, **C**-main group element), crystallize with a cubic symmetry ($F\bar{4}3m$). Their crystal structure can be perceived as an interpenetration of four face-centered cubic (fcc) lattices with four characteristic crystallographic sites in the unit cell: 4a (0, 0, 0) occupied by **A**, 4c (1/4, 1/4, 1/4) occupied by **B**, 4b (1/2, 1/2, 1/2) occupied by **C** atoms and the additional nominally unfilled tetrahedral 4d site (3/4, 3/4, 3/4). Ti-Rich $Ti_{1-x}M_xNiSn$ (M = Hf, Zr), as the lightest and cheapest among other n-type HHs, should be of great interest for practical applications, however, their relatively poor thermoelectric performance make them less attractive than other HH compositions.[9–11] Although, structural studies of TiNiSn and Ni-rich $TiNi_{1+x}Sn$ compounds, based on powder X-ray and neutron diffraction (PXD and PND, respectively) as well as scanning transmission electron microscopy (STEM) are quite vast,[4,6,12–21] there is a limited number of reports on substituted $Ti_{1-x}M_xNiSn$ in the Ti-rich region.[22–26] Considering that: i) understanding of the crystal structure is crucial for optimization of thermoelectric performance, and ii) Ti- and Ni-rich (Ti,Hf)NiSn phases are among the least-studied compositions, we have in this work synthesized and performed a comprehensive structural characterization of n-type compounds with the general formula $Ti_{1-x}Hf_xNi_ySn$, x = 0.00, 0.10, 0.15, 0.20 and y = 1.0, 1.1. Our previous investigation showed that high-quality diffraction data, in particular high-resolution, are indispensable for reliable crystallographic analysis of HH phases.[27] Thus, in the present study, all samples were examined by high-resolution synchrotron radiation powder X-ray diffraction (SR-PXD).

The reported PXD data for arc-melted and annealed (1073 K) $Ti_{1-x}Hf_xNiSn$, x = 0.00, 0.05, 0.10, 0.20, 0.30, 0.40, 0.50, showed formation of the HH phase but also small amounts of FH and Sn_5Ti_6.[22] Samples with x = 0.10 and 0.20 demonstrated reduced Seebeck coefficient (S) and the electrical conductivity (σ), in the range of 300–950 K. Higher Hf concentration (x = 0.30–0.50) increased the values of both parameters. The overall increase of the TE performance was explained by the Hf-induced reduction of the lattice thermal conductivity with no clarification of changes observed in the electric transport properties. Data for $Ti_{0.95}Hf_{0.05}NiSn$ and $Ti_{0.2}Hf_{0.8}NiSn$,[23] prepared by arc melting/spark plasma sintering and annealing at 1073 K, showed reduced electrical resistivity ($\rho = \sigma^{-1}$) in comparison to pure TiNiSn. The Hf presence decreased the Seebeck coefficient in both samples, however, much lower $|S|$ was observed for $Ti_{0.2}Hf_{0.8}NiSn$, indicating a higher intrinsic carrier concentration.[23] As expected, the thermal conductivity (κ) of both materials was also lower than that of TiNiSn. In other studies, $Ti_{1-x}Hf_xNiSn$, x = 0.25 and 0.50, were characterized by higher electrical resistivity than TiNiSn, however its lower value was observed in a sample with the higher Hf amount.[24] Interestingly, changes in S varied. While for $Ti_{0.75}Hf_{0.25}NiSn$, the observed $|S|$ were higher than for TiNiSn in the range of 300–850 K, for $Ti_{0.5}Hf_{0.5}NiSn$, S increased only slightly between 550 K and 700 K, suggesting a similar intrinsic carrier concentration. Hf substitution also lowered κ, which was similar in both samples. Recently, a $Ti_{1-x}Hf_xNiSn_{1-y}Sb_y$ sample series prepared by low-/high-temperature rapid solidification and spark plasma sintering, was investigated by PXD and STEM.[25] Diffraction data reported for as-solidified $Ti_{1-x}Hf_xNiSn$, x = 0.0, 0.2, 0.3, 0.4, 0.5, showed the presence of the HH phase in both low- and high-temperature processed powders. Additionally, FH, Sn_5Ti_6 and metallic Sn were detected. The sample phase compositions changed upon densification, resulting in formation of the phase-pure HH materials, in the low-temperature solidified powders. However, PXD measurements were carried out with a laboratory diffraction instrument (λ = Cu Kα), which due to possibly limited-resolution[27] may have generated data with insufficient quality for reliable phase analysis. STEM investigation of the local disorder in the same sample series showed fluctuation in the HH chemical composition, signaling a possible phase separation. These studies did not report nucleation of FH precipitates but demonstrated formation of the large local lattice strain originating from the presence of disorderly distributed Ni atoms, which induced (Ti,Hf)/Sn anti-site defects.[25]

In the research reported on the TiNiSn-based HH systems, the amount of Ni has been shown to affect the electric transport properties and, at the same time, reduce of the lattice thermal conductivity in the HH compounds.[9,10,14,19] Studies performed so far indicate that excess Ni either statistically occupies an available subset of tetrahedral interstitial sites (4d) in the HH structure and/or becomes a nucleation center of the full-Heusler phase(s).[14,15,19,28–31] In this work, through comprehensive investigation of long- and short-range atomic structures of the $Ti_{1-x}Hf_xNi_ySn$ HH phases, x = 0.00, 0.10, 0.15, 0.20 and y = 1.0, 1.1, we address three questions: 1) what is the nature of Hf-/Ni-related processes in the selected HH compounds, 2) what is the correlation between a long-range atomic order and a local atomic structure in HH phases, and 3) what is the relationship between the crystal chemistry/microstructure and electric transport properties of chosen compositions.

Experimental details

Synthesis and processing of materials

Two series of polycrystalline samples, with the following nominal compositions: $Ti_{1-x}Hf_xNiSn$ and $Ti_{1-x}Hf_xNi_{1.1}Sn$, x = 0.00, 0.10, 0.015, 0.20, were synthesized. Metallic pieces (Ti, Hf, Ni, Sn: Goodfellow, purity >99.5%) were first arc melted under Ar atmosphere, in a water-cooled cooper heart with a tungsten electrode. To improve sample homogeneity pellets were flipped and remelted several times. The obtained ingots were ball milled with an 8000D SPEX mixer for 6 minutes, at constant velocity of *ca.* 1000 rpm. Mechanochemical powder processing was carried out in stainless steel vials, with a ball-to-powder

weight ratio of 3 : 1. The resulting fine-grained powders were cold pressed into pellets, wrapped in Ta foil and subsequently sealed under Ar atmosphere in stainless steel tubes. The samples were then annealed at 950 °C for one week and eventually water quenched. Prior to characterization, the pellets were cut into smaller pieces with a diamond saw.

Characterization methods

High-resolution SR-PXD measurements of both as-cast and heat-treated materials were carried out at the Swiss-Norwegian Beamline, ESRF, Grenoble (France). Data were collected at the BM31 station, equipped with a high-resolution powder X-ray diffraction instrument (λ = 0.50218 Å, 2θ = 1–40°, point detector with analyzer crystals). The samples were crushed with a mortar to a fine powder and loaded in sealed 0.3 mm diameter boron-glass capillaries, which were rotated during measurements to improve powder averaging. The collected data were analyzed by Rietveld refinements using the Fullprof Suite program.[32] The analysis of Bragg scattering provided exhaustive information on the long-range order of the HH atomic structure, represented by the unit cell (*i.e.* the time- and space-averaged position of atoms). The diffraction profiles were modelled with a pseudo-Voigt peak shape function and the background was defined by interpolation between manually chosen points. The SR-PXD data of the $Ti_{1-x}Hf_xNiSn$ sample series were fitted against the Ni-rich model of the HH phase, which represented an averaged atomic arrangement within the HH matrix and included occupancy of the nominally unfilled 4d crystallographic position. Rietveld refinements of the SR-PXD patterns for the $Ti_{1-x}Hf_xNi_{1.1}Sn$ sample series were performed with an additional model of the FH crystal structure with an independent lattice parameter. For the identified HH/FH phase(s), the following parameters were allowed to vary during the refinement cycles: a scale factor, up to six profile parameters (U, V, W, mixing factor and two asymmetry parameters), a unit cell parameter, overall or individual displacement parameters, an occupancy factor for 4a, 4c/8c and 4d sites. Due to a high number of phases and/or poor crystallinity of the as-cast powders, the occupancy of the 4d interstice in the HH structure was refined only for the annealed samples. All data were corrected for X-ray absorption, which was calculated assuming a packing fraction of 0.5 in the capillaries.

The microstructure and chemical composition in the selected samples of the annealed $Ti_{1-x}Hf_xNiSn$ series were characterized by transmission electron microscopy (TEM) and annular bright field (ABF)/high-angle annular dark field (HAADF) scanning transmission electron microscopy (STEM) coupled to X-ray energy dispersive spectroscopy (EDS). As SR-PXD did not provide any information about short-ranged structural features, TEM was also applied to investigate a local atomic arrangement (*i.e.* a short-range atomic structure) in the chosen materials. This work was performed with a DCOR Cs probe-corrected FEI Titan G2 60-300 instrument, with 0.08 nm nominal spatial resolution when operated at 300 kV, equipped with a Bruker SuperX EDS system comprising four silicon drift detectors. TEM sample preparation involved depositing powder suspended in isopropanol on lacey carbon grids followed by shielded plasma cleaning. The local crystal structure and lattice strain were analyzed by performing fast Fourier transform (FFT) with the DiffTools[33] and geometric phase analysis (GPA) script packages, developed for Digital Micrograph (Gatan Inc).

The in-plane Seebeck coefficient and electrical resistivity were measured under Ar atmosphere using a custom made setup.[34] Each sample was measured over up to six heating–cooling cycles and pellets were not polished in between. In Fig. 8 only one full cycle is displayed for clarity, as no significant changes in the electric transport properties were observed. The thermal conductivity was not measured here, as the samples were only compacted by cold-pressing of powders, followed by conventional sintering, and were likely to deviate in their relative density, thus preventing a meaningful comparison.

Ab initio calculations

Density functional theory (DFT) was used to calculate the mixing energy of $Ti_{1-x}Hf_xNi_ySn$ as a function of y, for selected

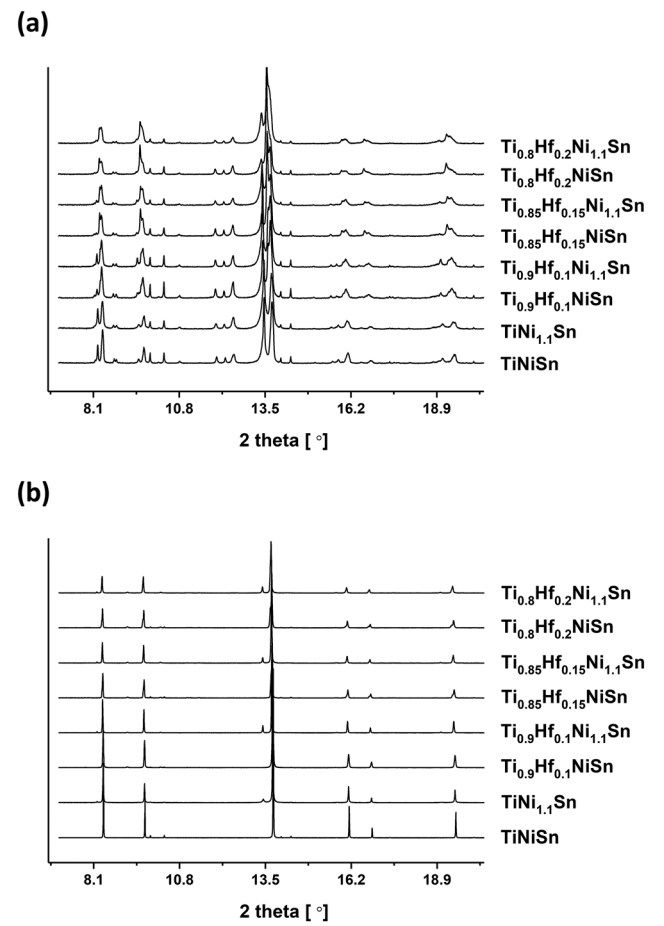

Fig. 1 High-resolution SR-PXD profiles (λ = 0.50218 Å) for the arc melted (a) and annealed (b) $Ti_{1-x}Hf_xNi_{1.0/1.1}Sn$ powders.

x values. A supercell approach was employed with the Vienna *ab initio* simulation package (VASP), a projector-augmented plane-wave code, with the Perdew–Burke–Ernzerhof (PBE) exchange–correlation function.[35,36] The recommended Ni maximum energy cutoff of 270 eV was utilized[35,36] and the structure was relaxed until interatomic forces became smaller than 0.02 eV $Å^{-1}$. For each composition, five 2 × 2 × 2 conventional unit cells were generated with a pseudo-random distribution of Hf/Ti substitutions and Ni interstitials. Semi-uniformity was imposed, by considering only subcell, where the number of Ni and Hf within each of 1 × 1 × 1 subcells could differ by no more than 1. For a given composition, only the supercell with the lowest mixing energy was retained.

Results and discussion

High-resolution synchrotron powder X-ray diffraction (SR-PXD) study

$Ti_{1-x}Hf_xNi_ySn$ as-cast samples. The high number of identified phases and poor crystallinity of the as-cast powders limited number of refined parameters during the Rietveld analysis (Table 1 and ESI†). Thus, as already mentioned in section Experimental details, the obtained compositional and structural information is only partial. Due to that, numbers listed in Table 1 represent a trend among identified phases in studied compositions and should not be treated as absolute values. The SR-PXD data of the arc melted TiNiSn and $TiNi_{1.1}$Sn show the formation of HH, FH, binary Sn_5Ti_6, Sn_3Ti_5 and metallic Sn (Fig. 1a, Table 1 and ESI†). The refined value of the HH unit cell parameter in $TiNi_{1.1}$Sn, a = 5.9504(1) Å, is slightly larger than in TiNiSn, a = 5.9484(2) Å, and both are significantly enlarged compared to the same phase present in the already reported annealed and/or hot-pressed/spark plasma sintered materials (~5.93 Å).[4,6,13,14,16–19,24,37] This is likely due to the higher degree of intrinsic disorder in their crystal structures, as commonly observed for phases formed in rapidly cooled/solidified powders. The FH lattice constant is identical in both samples, a = 6.0599(2) and 6.0596(2) Å for TiNiSn and $TiNi_{1.1}$Sn, respectively, and smaller than values reported for the annealed $TiNi_2Sn$ (a = 6.095(3) Å).[38] The Hf-containing samples crystallize with the same compounds as $TiNi_{1.0/1.1}$Sn, but a second HH phase is formed in addition. The observed phase compositions are in agreement with the theoretical predictions for the $Ti_{1-x}Hf_xNiSn$ system[39] and with the experimental results published for arc melted samples with the same compositions.[13,22,40] The unit cell parameters of $Ti_{1-x}Hf_xNiSn$ HHs formed in each sample differ slightly, which results from small deviations in their chemical compositions. Both phases are Ti-rich, but one of them has a higher amount of Ti (hereafter referred to as HH1 or Ti-enriched) than the other (hereafter referred to as HH2 or Hf-enriched). Interestingly, the HH phases formed in both investigated series exhibit almost the same Ti/Hf fraction at 4a sites (Table 1). The increasing amount of Hf reduces the occupancy of the 4a site by Ti in both HH structures (Table 1), and in turn, expands their unit cells. The results also demonstrate incorporation of Hf into the FH structure but show that increasing Hf content decreases the FH concentration in both sample series. A summary of the Rietveld refinement results is presented in Table 1.

$Ti_{1-x}Hf_xNi_ySn$ annealed samples. High-resolution SR-PXD data for the annealed $Ti_{1-x}Hf_xNi_{1.0/1.1}Sn$ materials indicate a tremendous change of the phase abundance in both sample series (Fig. 1–3, Table 2 and ESI†). Powder patterns of TiNiSn and $Ti_{0.9}Hf_{0.1}NiSn$ are indexed with a single HH phase that accounts for 95.2 and 95.4% of the sample mass, respectively. Apart from that, only small amounts of metallic Sn and HfO_2 are present in the samples (Table 2). The latter appears to form easily and has already been reported in Hf-based MNiSn powders.[17,27] The corresponding Ni-rich compositions tend to additionally form an ordered FH phase, whose fraction is highest in the Hf-free $TiNi_{1.1}Sn$ (9.8 *vs.* 6.8 wt% in $Ti_{0.9}Hf_{0.1}Ni_{1.1}Sn$). Its occurrence lowers the concentration of HH in both $TiNi_{1.1}Sn$ and $Ti_{0.9}Hf_{0.1}Ni_{1.1}Sn$ (89.7 and 91.5 wt%, respectively). The HH lattice constant in TiNiSn and $TiNi_{1.1}Sn$ is 5.93419(3) and 5.94226(3) Å, respectively. The slightly larger a value of the latter is likely to result from a higher degree of disorder in the crystal structure caused by the excess Ni. In both HHs, Ni occupies orderly the 4c site but its presence at 4d varies and corresponds to 5% and 8% in TiNiSn and $TiNi_{1.1}Sn$, respectively (Fig. 3 and Table 2). The a values as well as the fractions of disordered Ni atoms are in agreement with previous reports for nominally identical samples.[12,15,16,18,19]

The HH phases formed in $Ti_{0.9}Hf_{0.1}NiSn$ and $Ti_{0.9}Hf_{0.1}Ni_{1.1}Sn$ have similar averaged chemical compositions refined to $Ti_{0.906}Hf_{0.094}NiSn$ and $Ti_{0.925}Hf_{0.075}Ni_{1.09}Sn$, respectively (Fig. 2 and Table 2). Interestingly, Rietveld analysis does not suggest any extra Ni in the HH structure in the nominally stoichiometric sample. However, in $Ti_{0.925}Hf_{0.075}Ni_{1.09}Sn$, 9% of the 4d site is occupied by disorderly distributed Ni atoms. This could be a reason of the larger lattice constant obtained for this phase (a = 5.95402(6) Å), as compared to $Ti_{0.906}Hf_{0.094}NiSn$ (a = 5.94192(6) Å), despite a slightly lower fraction of Hf in the structure (Fig. 3). The FH phase formed in $Ti_{0.9}Hf_{0.1}Ni_{1.1}Sn$ does not show any Ni deficiency, as previously reported by Downie *et al.*[19]

SR-PXD patterns for $Ti_{0.85}Hf_{0.15}Ni_{1.0/1.1}Sn$ and $Ti_{0.8}Hf_{0.2}Ni_{1.0/1.1}Sn$ suggest that two Ti-rich HH phases (HH1 and HH2, see section $Ti_{1-x}Hf_xNi_ySn$ as-cast samples) and a small amount of HfO_2 are formed in both samples. The Ni-rich materials crystallize with an additional FH phase, while in the Ni-stoichiometric series, metallic Sn is observed in addition to the HH phases. HHs formed in corresponding samples of both series reveal similar refined compositions (see Table 2). An increasing amount of Hf reduces the number of Ti at the 4a site in the HH crystal structures but does not affect significantly the FH fraction formed in the Ni-rich samples. In $Ti_{0.85}Hf_{0.15}NiSn$, the small difference in lattice constants between HH1 and HH2 (a = 5.94969(8) Å *vs.* 5.9647(1) Å, respectively) can be attributed to the variation in the Hf/Ti ratio. The Rietveld refinements demonstrate that, while the 4c site is fully occupied by Ni atoms in both phases, the 4d position

Table 1 Lattice parameter (*a*), phase abundance, fractional occupancies (*n*), displacement parameters ($B_{iso}/B_{iso\_overall}$) and goodness-of-fit (χ^2) values for the $Ti_{1-x}Hf_xNi_ySn$ HH and FH phases in the as-cast samples obtained by Rietveld analysis of high-resolution SR-PXD data. Estimated standard deviations are given in parentheses

As-cast	TiNiSn	$TiNi_{1.1}Sn$	$Ti_{0.9}Hf_{0.1}NiSn$	$Ti_{0.9}Hf_{0.1}Ni_{1.1}Sn$	$Ti_{0.85}Hf_{0.15}NiSn$	$Ti_{0.85}Hf_{0.15}Ni_{1.1}Sn$	$Ti_{0.8}Hf_{0.2}NiSn$	$Ti_{0.8}Hf_{0.2}Ni_{1.1}Sn$
HH1 [wt%]	*48(1)*	*43(1)*	*37.6(6)*	*35(1)*	*36(1)*	34(1)	*36(1)*	*42(1)*
a [Å]	5.9484(2)	5.9504(1)	5.9666(3)	5.9705(4)	5.9750(4)	5.9758(5)	5.9818(6)	5.9850(7)
Refined composition	$TiNi_{0.948}Sn$	$TiNi_{0.938}Sn$	$Ti_{0.895}Hf_{0.105}NiSn$	$Ti_{0.885}Hf_{0.115}NiSn$	$Ti_{0.840}Hf_{0.160}NiSn$	$Ti_{0.850}Hf_{0.150}NiSn$	$Ti_{0.803}Hf_{0.197}NiSn$	$Ti_{0.803}Hf_{0.197}NiSn$
Atom (*n*)								
Ti (4a)	1.00(–)	1.00(–)	0.895(3)	0.885(5)	0.840(1)	0.850(5)	0.803(5)	0.803(5)
Hf (4a)	0.00(–)	0.00(–)	0.105(–)	0.115(–)	0.160(–)	0.150(5)	0.197(–)	0.197(–)
Sn (4b)	1.00(–)	1.00(–)	1.00(–)	1.00(–)	1.00(–)	1.00(–)	1.00(–)	1.00(–)
Ni (4c)	0.948(8)	0.938(8)	1.00(–)	1.00(–)	1.00(–)	1.00(–)	1.00(–)	1.00(–)
$B_{iso\_overall}$ [Å^2]	0.61(3)	0.77(1)	0.12(4)	0.12(6)	0.03(5)	0.12(5)	0.16(5)	0.11(4)
HH2 [wt%]	—	—	*15.5(6)*	*15(1)*	*29(1)*	*25(1)*	*34(1)*	*20(1)*
a [Å]	—	—	6.0033(3)	6.0039(4)	6.0156(3)	6.0145(4)	6.0231(3)	6.0210(3)
Refined composition	—	—	$Ti_{0.81}Hf_{0.19}NiSn$	$Ti_{0.83}Hf_{0.17}NiSn$	$Ti_{0.718}Hf_{0.282}NiSn$	$Ti_{0.738}Hf_{0.262}NiSn$	$Ti_{0.61}Hf_{0.39}NiSn$	$Ti_{0.64}Hf_{0.36}NiSn$
Atom (*n*)								
Ti (4a)	—	—	0.81(1)	0.83(1)	0.718(8)	0.738(8)	0.61(1)	0.64(2)
Hf (4a)	—	—	0.19(–)	0.17 (–)	0.282(–)	0.262(–)	0.39(–)	0.36(–)
Sn (4b)	—	—	1.00(–)	1.00(–)	1.00(–)	1.00(–)	1.00(–)	1.00(–)
Ni (4c)	—	—	1.00(–)	1.00(–)	1.00(–)	1.00(–)	1.00(–)	1.00(–)
$B_{iso\_overall}$ [Å^2]	—	—	1.1(1)	1.2(2)	0.66(7)	1.0(1)	0.70(6)	1.0(1)
FH1 [wt%]	*36(1)*	*41(1)*	*26.9(5)*	*36.2(8)*	15.6(5)	*26.6(6)*	*14.5(5)*	*25.1(6)*
a [Å]	6.0599(2)	6.0596(1)	6.0776(3)	6.0814(3)	6.0906(6)	6.0886(5)	6.0942(7)	6.0929(5)
Refined composition	$TiNi_2Sn$	$TiNi_2Sn$	$Ti_{0.855}Hf_{0.145}Ni_2Sn$	$Ti_{0.850}Hf_{0.150}Ni_2Sn$	$Ti_{0.80}Hf_{0.20}Ni_2Sn$	$Ti_{0.783}Hf_{0.217}Ni_2Sn$	$Ti_{0.76}Hf_{0.24}Ni_2Sn$	$Ti_{0.755}Hf_{0.245}Ni_2Sn$
Atom (*n*)								
Ti (4a)	1.00(–)	1.00(–)	0.855(5)	0.850(1)	0.80(1)	0.783(8)	0.76(2)	0.755(8)
Hf (4a)	0.00(–)	0.00(–)	0.145(–)	0.150(–)	0.20(1)	0.217(–)	0.24(2)	0.245(–)
Sn (4b)	1.00(–)	1.00(–)	1.00(–)	1.00(–)	1.00(–)	1.00(–)	1.00(–)	1.00(–)
Ni (8c)	1.00(–)	1.00(–)	1.00(–)	1.00(–)	1.00(–)	1.00(–)	1.00(–)	1.00(–)
$B_{iso\_overall}$ [Å^2]	1.07(4)	1.01(4)	0.62(6)	0.83(5)	0.66(9)	0.63(6)	0.7(1)	0.41(6)
Sn [wt%]	*3.1(1)*	*2.0(1)*	*3.3(1)*	*2.3(1)*	*3.4(2)*	*2.1(2)*	*3.4(2)*	*2.0(1)*
Sn_5Ti_6 [wt%]	*6.6(3)*	*8.5(4)*	*8.5(4)*	*6.0(4)*	*8.0(6)*	*6.1(6)*	*4.7(8)*	*6.3(7)*
Sn_3Ti_5 [wt%]	*6.3(3)*	*5.5(3)*	*8.2(4)*	*5.5(3)*	*8.0(4)*	*6.2(5)*	*7.4(5)*	*4.5(4)*
χ^2	2.67	2.06	2.94	3.19	2.84	2.50	2.99	2.45

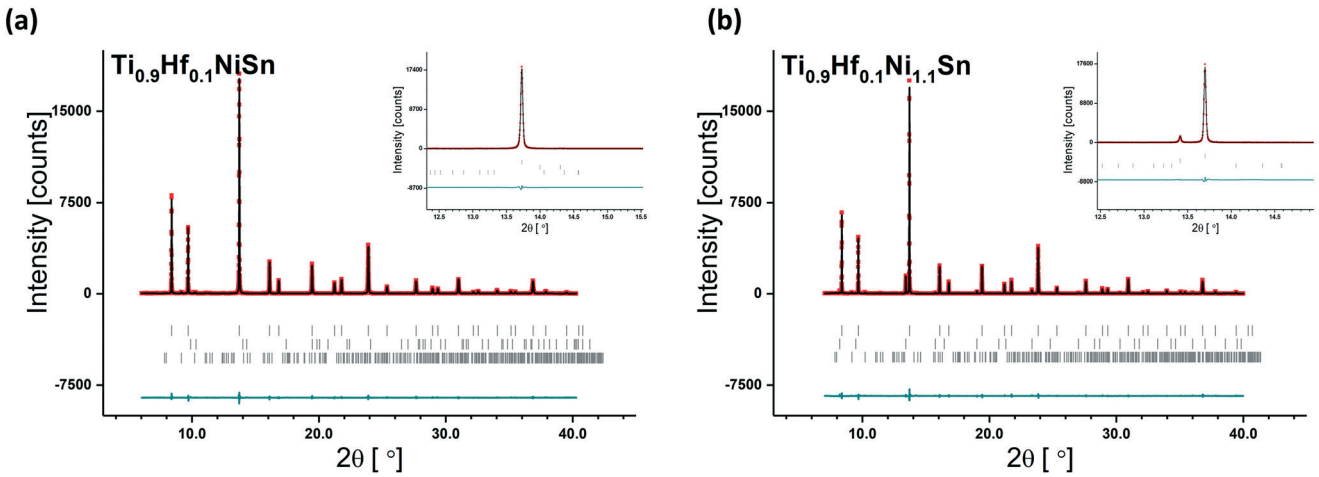

Fig. 2 Observed (dots), calculated (line) and difference (bottom line) high-resolution SR-PXD patterns (λ = 0.50218 Å) obtained for annealed $Ti_{0.9}Hf_{0.1}NiSn$ (a) and $Ti_{0.9}Hf_{0.1}Ni_{1.1}Sn$ (b). Vertical bars indicate Bragg peaks positions of contributing phases, from top to bottom: (a) HH, Sn, HfO_2; (b) HH, FH, HfO_2.

is filled to much lesser extent. Only 4% and 1% of the site is disorderly populated by Ni in the crystal structure of HH1 and HH2, respectively (Table 2 and Fig. 3).

In nominal $Ti_{0.85}Hf_{0.15}Ni_{1.1}Sn$, 7.4 wt% of FH is formed at the expense of the Hf-enriched HH2 (14 wt%). Its presence increases the amount of HH1 by 6 wt% and rises the fraction of interstitial Ni from 4% to 10%, compared to $Ti_{0.85}Hf_{0.15}NiSn$. While the unit cell parameters of HH2 (Table 2) are almost the same in $Ti_{0.85}Hf_{0.15}NiSn$ and $Ti_{0.85}Hf_{0.15}Ni_{1.1}Sn$, the a value for HH1 in the Ni-rich composition is somewhat larger. This could result from a slightly higher Hf and/or extra interstitial Ni fraction in the crystal structure.

The abundance of phases in nominal $Ti_{0.8}Hf_{0.2}NiSn$ is comparable to that of $Ti_{0.85}Hf_{0.15}NiSn$, with a small increase in HH2, which takes place at the expense of HH1 (Table 2). The reduced amount of Ti in both structures leads to an expansion of their unit cells (a = 5.95511(8) and 5.9738(1) Å for HH1 and HH2, respectively). The higher amount of Hf in HH1 raises the fraction of interstitial Ni populating the 4d site, as compared to HH1 of $Ti_{0.85}Hf_{0.15}NiSn$. However, it does not affect the occupancy of this site in HH2. Though, the phase composition of $Ti_{0.8}Hf_{0.2}Ni_{1.1}Sn$ is the same as of $Ti_{0.85}Hf_{0.15}Ni_{1.1}Sn$, the fraction of compounds present varies (Table 2). The FH phase crystallizes at the cost of Ti-enriched HH1 and its amount is higher than in $Ti_{0.85}Hf_{0.15}Ni_{1.1}Sn$. At the same time, in the Ni-rich $Ti_{0.8}Hf_{0.2}Ni_{1.1}Sn$ the fraction of Ti-enriched HH1 and amount of extra Ni at the 4d site is higher than in $Ti_{0.8}Hf_{0.2}NiSn$.

The obtained results suggest that the single, thermodynamically stable $Ti_{1-x}Hf_xNi_ySn$ HH phase crystallizes exclusively in samples with the following nominal compositions: TiNiSn/$TiNi_{1.1}Sn$ and $Ti_{0.9}Hf_{0.1}NiSn$/$Ti_{0.9}Hf_{0.1}Ni_{1.1}Sn$. The solubility limit of Hf in TiNiSn and $TiNi_{1.1}Sn$ is not affected by the Ni amount. The experimental range of the $Ti_{1-x}Hf_xNi_{1.0/1.1}Sn$ solid solution in the Ti-rich system is $0 < x < 0.15$ at 1223 K and appears more restricted than the solubility regions suggested earlier by empirical ($Ti_{0.74}Hf_{0.26}NiSn$ at 1273 K)[37,41] and theoretical studies ($Ti_{0.83}Hf_{0.17}NiSn$ at 1273 K,[39] miscibility over the whole composition range at 500 K (ref. 42) or 700 K (ref. 43)). For samples with $x \geq 0.15$, formation of two Hf-incorporating HH phases is observed. Both compounds are Ti-rich and separation into more abundant Ti-enriched (HH1) and less abundant Hf-enriched (HH2) compositions is observed. In the $Ti_{1-x}Hf_xNiSn$ samples, excess Ni is associated exclusively with the HH phase as no FH is formed. Ni atoms are distributed disorderly at the nominally vacant 4d site in the HH crystal structure. In the Ni-rich compositions, segregation of the FH phase takes place. In $Ti_{0.9}Hf_{0.1}Ni_{1.1}Sn$ and $Ti_{0.85}Hf_{0.15}Ni_{1.1}Sn$, FH accommodates less Ni (6.8 and 7.4%, respectively) than the 4d sites in the HH structures (~9% occupancy). However, in $Ti_{0.8}Hf_{0.2}Ni_{1.1}Sn$ the opposite trend is observed (8.7% of FH *vs.* 7.8% of Ni at the 4d site in HH). Interestingly, in all Ti-enriched compositions, regardless of the nominal Ni amount, higher percentage of Ni occupies the 4d site (4–10%) than in Hf-enriched phases (0–4%). The presence of Hf in the Ni-rich samples also hinders crystallization of the FH phase as compared to $TiNi_{1.1}Sn$. The abundance of HfO_2 in the $Ti_{1-x}Hf_xNiSn$ sample series is rather constant, while its concentrations rises in $Ti_{1-x}Hf_xNi_{1.1}Sn$ as the Hf amount increases (1.7 wt% and 3.64 wt% in $Ti_{0.9}Hf_{0.1}Ni_{1.1}Sn$ and $Ti_{0.8}Hf_{0.2}Ni_{1.1}Sn$, respectively). Metallic Sn, present only in the $Ti_{1-x}Hf_xNiSn$ sample series, gradually disappears with a higher fraction of Hf in the sample (2.0 wt% and 0.67 wt% in $Ti_{0.9}Hf_{0.1}NiSn$ and $Ti_{0.8}Hf_{0.2}NiSn$, respectively). Its concentration in the TiNiSn and $TiNi_{1.1}Sn$ samples is the same and equals 0.45 wt%. A summary of the Rietveld refinements is presented in Table 2.

DFT calculations

The DFT calculations were performed to get a better insight into the observed preferential distribution of Ni atoms over compositionally different HH phases. The simulations

Table 2 Lattice parameter (a), phase abundance, fractional occupancies (n), displacement parameters (B_{iso}/$B_{iso\_overall}$) and goodness-of-fit (χ^2) values for the $Ti_{1-x}Hf_xNi_ySn$ HH and FH phases in the annealed samples obtained by Rietveld analysis of high-resolution SR-PXD data. Estimated standard deviations are given in parentheses

Annealed	TiNiSn	$TiNi_{1.1}Sn$	$Ti_{0.9}Hf_{0.1}NiSn$	$Ti_{0.9}Hf_{0.1}Ni_{1.1}Sn$	$Ti_{0.85}Hf_{0.15}NiSn$	$Ti_{0.85}Hf_{0.15}Ni_{1.1}Sn$	$Ti_{0.8}Hf_{0.2}NiSn$	$Ti_{0.8}Hf_{0.2}Ni_{1.1}Sn$
HH1 [wt%]	*95.2(7)*	*89.7(5)*	*95.4(2)*	*91.5(6)*	*70.1(9)*	*76(2)*	*66.0(9)*	*69(1)*
a [Å]	5.93419(3)	5.94226(3)	5.94192(6)	5.95402(6)	5.94969(8)	5.9590(1)	5.95511(8)	5.9640(1)
Refined composition	$TiNi_{1.048}Sn$	$TiNi_{1.083}Sn$	$Ti_{0.906}Hf_{0.094}NiSn$	$Ti_{0.925}Hf_{0.075}Ni_{1.090}Sn$	$Ti_{0.916}Hf_{0.084}Ni_{1.044}Sn$	$Ti_{0.898}Hf_{0.102}Ni_{1.095}Sn$	$Ti_{0.881}Hf_{0.119}Ni_{1.060}Sn$	$Ti_{0.873}Hf_{0.127}Ni_{1.078}Sn$
Atom (n)/B_{iso} [Å^2]								
Ti (4a)	1.00(−)/0.22(5)	1.00(−)/0.36(4)	0.906(3)/0.32(4)	0.925(3)/0.30(4)	0.916(2)/0.23(5)	0.898(3)/0.43(5)	0.881(3)/0.34(5)	0.873(3)/0.36(5)
Hf (4a)	0.00(−)/—	0.00(−)/—	0.094(−)/0.32(−)	0.075(−)/0.30(−)	0.084(−)/0.23(−)	0.102(−)/0.43(−)	0.119(−)/0.34(−)	0.127(−)/0.36(−)
Sn (4b)	1.00(−)/0.33(2)	1.00(−)/0.56(2)	1.00(−)/0.38(2)	1.00(−)/0.42(2)	1.00(−)/0.42(3)	1.00(−)/0.49(3)	1.00(−)/0.33(3)	1.00(−)/0.58(4)
Ni (4c)	1.00(−)/0.32(−)	1.00(−)/0.41(−)	1.00(−)/0.32(−)	1.00(−)/0.40(−)	1.00(−)/0.31(−)	1.00(−)/0.48(−)	1.00(−)/0.39(−)	1.00(−)/0.45(−)
Ni (4d)	0.048(1)/0.32(4)	0.083(1)/0.41(3)	0.00(−)/0.32(3)	0.090(5)/0.40(4)	0.044(5)/0.31(4)	0.095(5)/0.48(4)	0.060(5)/0.39(5)	0.078(5)/0.45(4)
HH2 [wt%]	—	—	—	—	*26.1(7)*	*14(1)*	*30.6(8)*	*19(1)*
a [Å]	—	—	—	—	5.9647(1)	5.9678(2)	5.9738(1)	5.9745(2)
Refined composition	—	—	—	—	$Ti_{0.818}Hf_{0.182}Ni_{1.014}Sn$	$Ti_{0.83}Hf_{0.17}NiSn$	$Ti_{0.758}Hf_{0.242}Ni_{1.011}Sn$	$Ti_{0.73}Hf_{0.27}Ni_{1.04}Sn$
Atom (n)/B_{iso} [Å^2]								
Ti (4a)	—	—	—	—	0.818(6)/0.4(1)	0.83(5)/0.4(3)	0.758(7)/0.3(1)	0.73(1)/0.2(1)
Hf (4a)	—	—	—	—	0.182(−)/0.4(−)	0.17(−)/0.4(−)	0.242(−)/0.3(−)	0.27(−)/0.2(−)
Sn (4b)	—	—	—	—	1.00(−)/0.9(1)	1.00(−)/1.4(3)	1.00(−)/1.1(1)	1.00(−)/0.5(2)
Ni (4c)	—	—	—	—	1.00(−)/0.53(−)	1.00(−)/0.4(−)	1.00(−)/0.55(−)	1.00(−)/0.25(−)
Ni (4d)	—	—	—	—	0.014(8)/0.53(7)	0.00(−)/0.4(2)	0.011(6)/0.55(7)	0.04(2)/0.25(9)
FH1 [wt%]	—	*9.8(2)*	—	*6.8(1)*	—	*7.4(2)*	—	*8.7(2)*
a [Å]	—	6.0739(2)	—	6.0799(1)	—	6.0824(1)	—	6.0851(1)
Refined composition	—	$TiNi_2Sn$	—	$Ti_{0.922}Hf_{0.078}Ni_2Sn$	—	$Ti_{0.930}Hf_{0.070}Ni_{1.92}Sn$	—	$Ti_{0.952}Hf_{0.047}Ni_{1.90}Sn$
Atom (n)								
Ti (4a)	—	1.00(−)	—	0.922(1)	—	0.930(8)	—	0.953(5)
Hf (4a)	—	0.00(−)	—	0.078(−)	—	0.070(−)	—	0.047(−)
Sn (4b)	—	1.00(−)	—	1.00(−)	—	1.00(−)	—	1.00(−)
Ni (8c)	—	1.00(−)	—	1.00(−)	—	0.96(3)	—	0.95(1)
$B_{iso\_overall}$ [Å^2]		2.0(1)		1.19(8)		1.2(2)		1.07(6)
Sn [wt%]	*0.45(3)*	*0.45(3)*	*2.0(1)*	—	*0.95(3)*	—	*0.67(3)*	—
HfO_2 [wt%]			*2.60(5)*	*1.7(2)*	*2.88(5)*	*3.1(1)*	*2.69(6)*	*3.64(7)*
χ^2	2.69	1.56	1.34	1.86	1.42	1.22	1.60	1.17

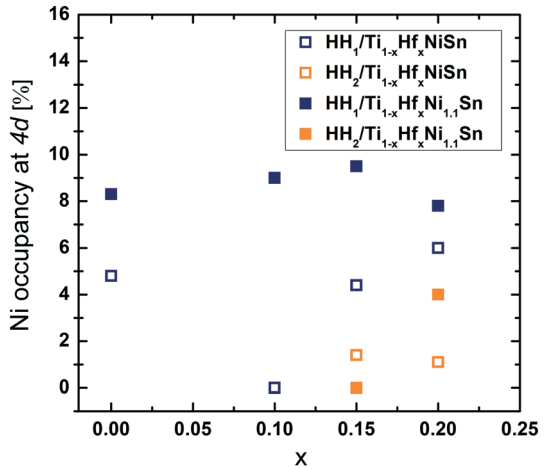

Fig. 3 The refined occupancy of the 4d site by Ni atoms in the HH1 and HH2 phases presented as a function of the Hf concentration in nominal $Ti_{1-x}Hf_xNi_{1.0/1.1}Sn$.

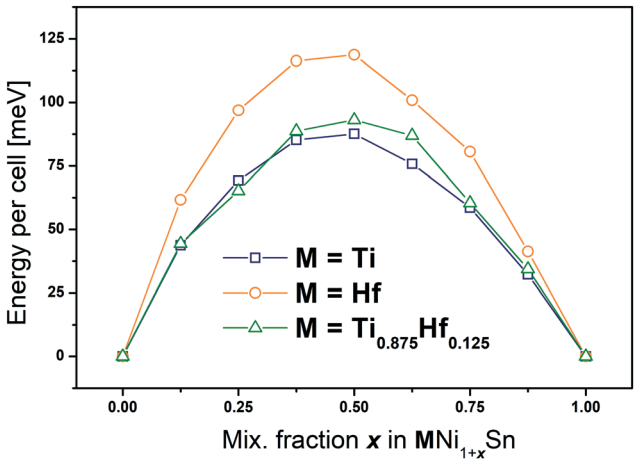

Fig. 4 DFT formation energies per unit cell relative to HH and FH end states for $MNi_{1+x}NiSn$, where x = Ni.

spanned three systems: the parental $TiNi_{1+x}Sn$ and $HfNi_{1+x}Sn$ as well as the substituted $Ti_{0.875}Hf_{0.125}Ni_{1+x}Sn$ (x = 0.000, 0.125, 0.250, 0.375, 0.500, 0.625, 0.750, 0.875, 1.000), which represented the average HH composition among the refined stoichiometries. The formation energies (Fes) obtained by DFT, relative to HH and FH, are positive for all studied configurations and point to the thermodynamic instability of the solid solution and/or ordered arrangement of Ni atoms/vacancies between x = 0 and 1 at 0 K. The values are highest for $HfNi_{1+x}Sn$, while those for $TiNi_{1+x}Sn$ and $Ti_{0.875}Hf_{0.125}Ni_{1+x}Sn$ are significantly lower (Fig. 4) and rather similar. In all systems, FEs are rising with increasing concentration of extra Ni in the HH crystal structure and exhibit a slight asymmetry around x = 0.5. This is most pronounced for HfNiSn. Such behavior suggests that the cost associated with insertion of Ni atoms into the vacant sublattice in the HH phase is slightly higher than formation of less costly Ni vacancies in the FH crystal structure. Although, our experimentally studied HH compositions reveal only small difference in Ti/Hf concentrations, the observed higher fraction of the disordered Ni atoms at the 4d site in the Ti-enriched phases follow the theoretically predicted pattern.

Transmission electron microscopy (TEM) study

High-resolution S/TEM was used to further investigate the grain morphology, chemical composition and local atomic arrangement in selected powders of the annealed $Ti_{1-x}Hf_xNiSn$ series, x = 0.10, 0.15 and 0.20. The studied samples exhibit a broad distribution of particle sizes, ranging from a few nm to a few μm. The grains of the HH phases are typically submicrometer-sized and show surface oxidation in addition to embedded nanoinclusions, likely to result from precipitation. The density, size and chemical composition of the precipitates vary among samples and appear to depend on Hf concentration (ESI†). EDS analysis of $Ti_{0.9}Hf_{0.1}NiSn$ reveals the presence of Sn, TiO_2 and HfO_2 nanoinclusions (Fig. 5 and ESI†). The latter are most abundant in the HH matrix and present spherical morphologies (Fig. 5 and 6). The shape of these nanoparticles, with sizes up to 80 nm, suggests isotropic endotaxial nucleation/growth within HHs. Indexation of the FFT of HAADF images shows that the phases adopt the $(20\bar{2})_{HfO_2}//(002)_{HHmatrix}$ and $[101]_{HfO_2}//[\bar{1}10]_{HHmatrix}$ orientation relationship, assuming the monoclinic oxide symmetry. The HfO_2/HH interface is semicoherent with the local strain concentrated in misfit dislocations (Fig. 6). Presence of HfO_2 precipitates, in the form of both embedder nanoinclusions and particles dispersed at HH grain boundaries, has already been reported for the p- and n-type half-Heusler systems and their structural characterization revealed monoclinic symmetry, the same as HfO_2 observed by SR-PXD in the present study.[44–46] However, here the atomic arrangement of the crystalline HfO_2 nanoprecipitates appears to have a higher symmetry than the one of the relaxed oxide structure. It resembles the tetragonal distortion already reported for the full-Heusler nanoinclusions in TiNiSn.[21] Analysis of the high-resolution SR-PXD data of this powder does not show any disorderly distributed Ni in the HH crystal structure or segregated FH phase, which is consistent with the TEM results as neither Ni-rich HH regions nor FH (nano)precipitates are observed.

In the $Ti_{0.8}Hf_{0.2}NiSn$ specimens, high-resolution TEM (HRTEM) reveals 'mosaic'-like domains, which represent the short-range atomic order. These regions, with sizes up to 20 nm, consist of different orientation variants of the underlying HH structure (Fig. 7a). Fast Fourier transforms of adjacent domains in $\langle 110\rangle_{HH}$ lattice images show extra spots due to a local periodicity of $1/3\langle 111\rangle$, not existing in the pristine HH phase (Fig. 7a and b). This highly ordered local atomic configuration corresponds to the presence/absence of sets of atoms parallel to {111} planes. The atomic positions associated with this periodicity may correspond to the nominally vacant 4d site, which from the analysis of the long-range atomic order, is known to be partly occupied by Ni (Table 2). Therefore, by combining information on the long-range HH structure, as obtained by SR-PXD, with the observed short-range atomic correlations, two structural models with

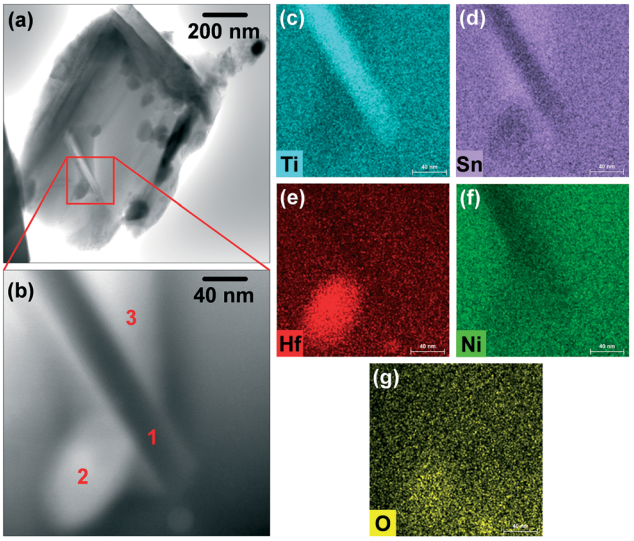

Fig. 5 (a) Low magnification HAADF STEM image of $Ti_{0.9}Hf_{0.1}NiSn$; (b) inset with ABF STEM image of HH particle with precipitates; 1 – TiO_2, 2 – HfO_2, 3 – Sn; (c–g) corresponding elemental EDS maps.

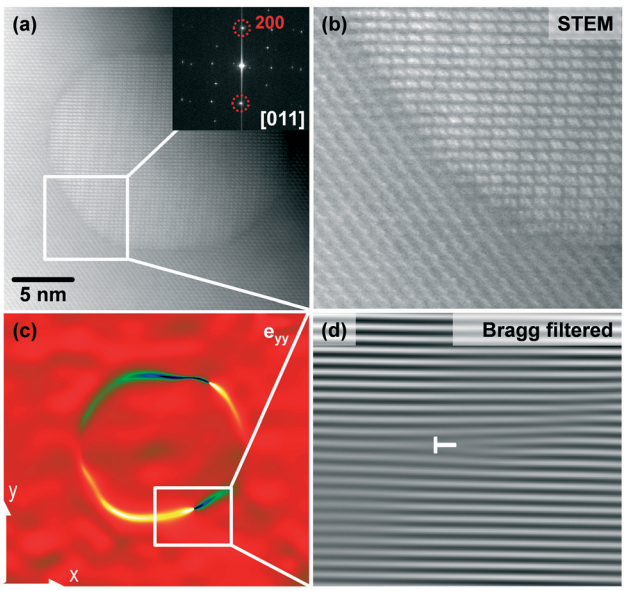

Fig. 6 (a) STEM-HAADF image of $Ti_{0.9}Hf_{0.1}NiSn$ showing HfO_2 nano-precipitate embedded in the HH matrix and corresponding fast Fourier transform with encircled common reflections of the HH and HfO_2 phases; (b) magnified region of the semicoherent HH/HfO_2 interface; (c) geometric phase analysis (GPA) image showing strain localization at the HH/HfO_2 phase boundary; (d) Bragg filtered image emphasizing the dislocation position.

variable Ni distribution are suggested. The first proposes that every third subset of the available 4d sites in the HH crystal structure is populated by Ni and corresponds to a defective HH phase (Fig. 7c). In the second model, the Ni atomic arrangement resembles the one in MNi_2Sn (FH) but with one in six of the Ni sites (8c) becoming vacant (Fig. 7d). This one represents a defective FH structure. The occurrence frequency of the occupied crystallographic positions suggests the following stacking sequence of $\{\bar{1}11\}$ planes: HH–HH–FH–HH–HH–FH… and FH–FH–HH–FH–FH–HH… for the defective half-Heusler and full-Heusler models, respectively. Comparison of the experimental data with simulated electron diffraction patterns (Fig. 7c and d), for the proposed Ni atomic configurations, does not allow to distinguish between the defects present in the $Ti_{0.8}Hf_{0.2}NiSn$ sample. However, both models demonstrate that the local ordering of Ni atoms could be responsible for the formation of the modulated structure observed by HRTEM. The performed DFT calculations also do not indicate one energetically favored atomic configuration as the formation energies for the defective HH and FH structures are very similar (Fig. 4).

The local atomic correlations, clearly seen at the nanometric scale, do not show long-range periodicity as no superstructure peaks are present in the $Ti_{0.8}Hf_{0.2}NiSn$ diffraction pattern. Still, the findings evidence a complex nature of interatomic correlations in the HH crystal structure, with excess Ni possibly occupying the nominally unfilled 4d sites. The observations demonstrate that interstitial Ni in the $Ti_{1-x}Hf_xNiSn$ HH structure may form locally ordered Ni-rich stacking faults, whose arrangement resembles the FH phase. The modulated domains observed in the present work differ from previous S/TEM studies reporting Ni-rich FH nano-inclusions in TiNiSn (ref. 21 and 47) and domains with distinct random arrangements of Ni at both the 4c and 4d sites in $Ti_{1-x}Hf_xNiSn$.[25] They are also unlike modulated structures in ZrNiSn and $Zr_{0.5}Hf_{0.5}NiSn$, where a variable local occupation of structural vacancies by excess Ni resulted from a spinodal decomposition.[48] However, the nature of the observed in this work short-range atomic structures bares similarities with the modulated Heusler-based shape memory martensites.[49] While the modulation in martensitic phases arises due to shuffling of the (110) FH planes in the $[1\bar{1}0]$ direction, which results in extra satellites on the rows of 110 reflections; here, the mechanism that generates extra satellites on the rows of 111 reflections is most likely diffusional rather than displacive.

Electric transport properties

Temperature dependence of the Seebeck coefficient ($S(T)$) and electrical resistivity ($\rho(T)$) was measured for the annealed samples, in the range of 300–750 K (Fig. 8 and Table 3). The obtained values were then used to calculate the thermoelectric power factor (PF = S^2/ρ). The measured $S(T)$ and $\rho(T)$ for both sample series are shown in Fig. 9. Regardless of the Ni amount, all samples show relatively large, negative values of $S(T)$, $|-150| \leq S(T)_{max} \leq |-190|$ μV K^{-1}, and the decrease of ρ with increasing temperature. As compared to the literature, $S(T)_{max}$ and $\rho_{max}(T)$ for TiNiSn and $TiNi_{1.1}Sn$ are within the range of values reported for the same nominal compositions.[4,12,14–20,24] The thermal conductivity was not measured for studied materials, as the powders were only compacted by cold-pressing, followed by conventional sintering, and were likely to deviate in their relative density, thus preventing a meaningful comparison.

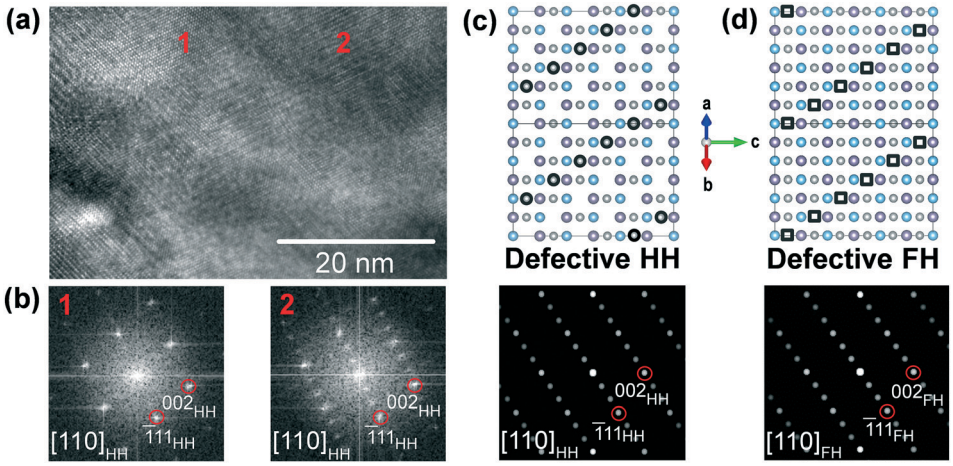

Fig. 7 (a) HRTEM image of the $Ti_{0.8}Hf_{0.2}NiSn$ particle with a mosaic-like modulated local structures; (b) FFT images of the pristine (1) and modulated (2) HH crystal lattices; (c and d) simulated electron diffraction patterns (bottom) and corresponding schematic illustrations of the defective HH/FH crystal structures with the proposed stacking sequence of the $(\bar{1}11)$ planes; violet: Sn, blue: Ti, grey: Ni atoms; black atoms in (c) represent the extra interstitial Ni atoms at the 4d site in the defective HH; black squares in (d) represent the vacant Ni positions in the defective FH.

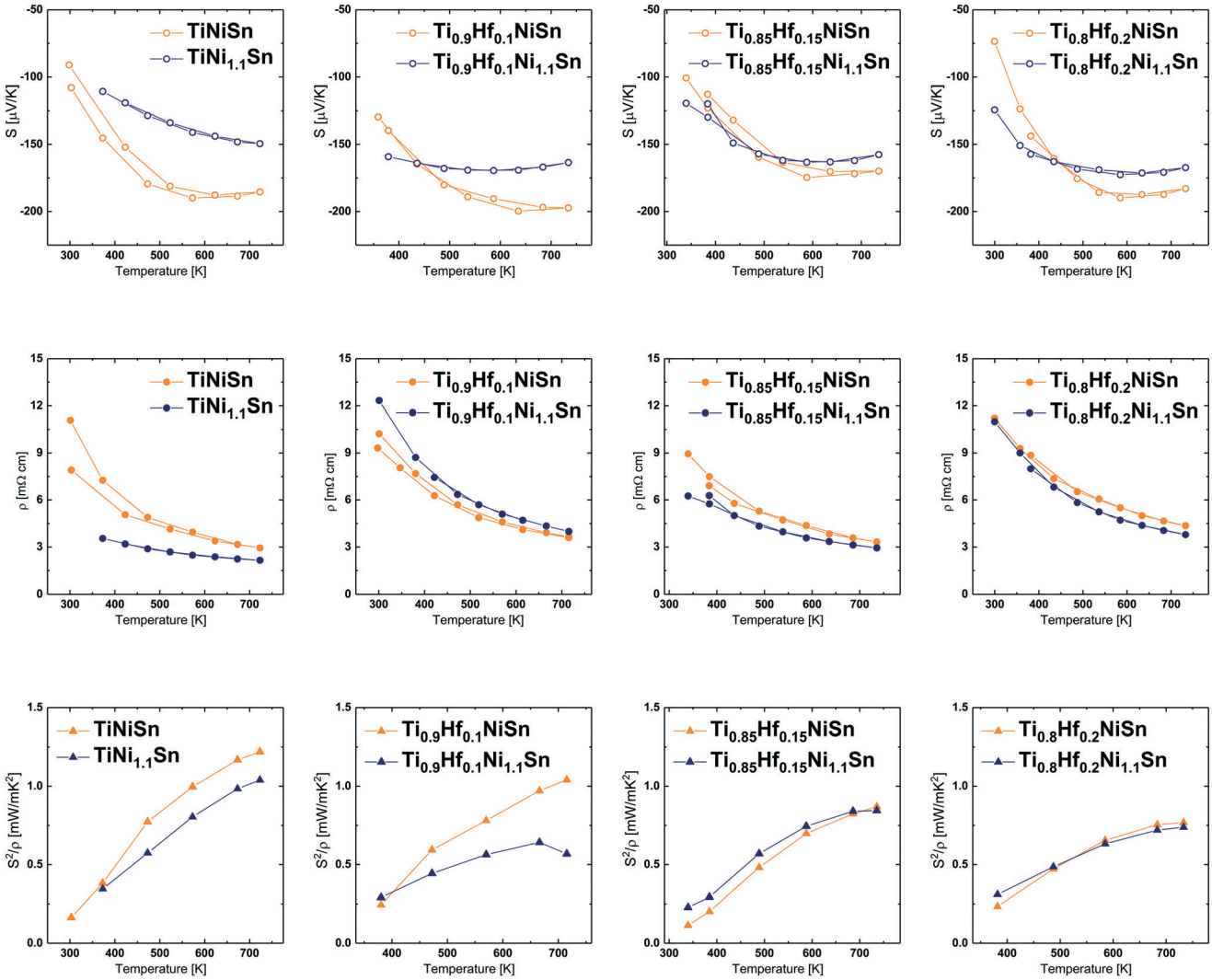

Fig. 8 The temperature dependence of the Seebeck coefficient (S, upper row), electrical resistivity (ρ, middle row) and thermoelectric power factor (S^2/ρ, bottom row) for the $Ti_{1-x}Hf_xNi_{1.0/1.1}Sn$ sample series. For $S(T)$ and $\rho(T)$ only one full heating–cooling cycle is presented for the clarity.

Table 3 Selected values of the Seebeck coefficient (S), electrical resistivity (ρ) and power factor (S^2/ρ) for the annealed $Ti_{1-x}Hf_xNi_ySn$ sample series

	TiNiSn	$TiNi_{1.1}Sn$	$Ti_{0.9}Hf_{0.1}NiSn$	$Ti_{0.9}Hf_{0.1}Ni_{1.1}Sn$	$Ti_{0.85}Hf_{0.15}NiSn$	$Ti_{0.85}Hf_{0.15}Ni_{1.1}Sn$	$Ti_{0.8}Hf_{0.2}NiSn$	$Ti_{0.8}Hf_{0.2}Ni_{1.1}Sn$
S_{max} [μV K^{-1}]	−190 (570 K)	−150 (730 K)	−200 (635 K)	−170 (587 K)	−175 (587 K)	−163 (587 K)	−190 (587 K)	−172 (587 K)
$S_{380\ K}$ [μV K^{-1}]	−145	−111	−140	−160	−123	−130	−144	−157
$S_{730\ K}$ [μV K^{-1}]	−185	−150	−197	−164	−170	−154	−183	−167
$\rho_{380\ K}$ [mΩ cm]	5.54	3.55	7.68	8.71	7.49	5.75	8.85	7.99
$\rho_{min(730K)}$ [mΩ cm]	2.94	2.15	3.64	3.99	3.32	2.94	4.36	3.79
S^2/ρ_{max}	1.22	1.04	1.04	0.64	0.87	0.84	0.77	0.74

The $S(T)$ plots for the $Ti_{1-x}Hf_xNiSn$ and $Ti_{1-x}Hf_xNi_{1.1}Sn$ sample series show the same trend with the temperature rise. However, the $S(T)$ dependence for the Ni-rich compositions is weaker than that for nominally stoichiometric samples, as reflected in a flat shape of the corresponding $S(T)$ curves: all nominally Ni-stoichiometric compositions show a smaller thermopower at 380 K than their Ni-rich counterparts, but the opposite trend is observed at 730 K. No systematic variation of the Seebeck coefficient with the nominal Hf concentration is observed, which is in agreement with previous reports.[22,25] Furthermore, the thermopower of the Ni-stoichiometric samples goes through a broad maximum, usually attributed to the onset of intrinsic conductivity, but no clear correlation of the Hf fraction and the temperature of maximum thermopower could be confirmed. The electrical resistivity of both sample series follows roughly the trend of the Seebeck coefficient: at constant temperature, when the thermopower decreases, the resistivity also decreases (Fig. 10), as expected for samples with different charge carrier concentrations. Unfortunately, we were not able to obtain meaningful Hall effect measurements for the current sample series, probably a consequence of the relatively low densification. However, it is easily understood that isovalent substitution of Ti by Hf at the 4a site does not lead to a systematic variation of the charge carrier concentration, with unintentional impurities as the main source of charge carriers in the present samples. On the other hand, we also note that interstitial Ni is not necessarily an efficient dopant in MNiSn, as has been rationalized by the Zintl–Klemm formalism,[2] which explains the similar values of Seebeck coefficient and resistivity independent of the nominal Ni content. Excess Ni forms rather an impurity band within the fundamental band gap, resulting in only a small increase of the carrier concentration and in turn, the flatter $S(T)$ curves as compared to the Ni-stoichiometric series.[2,19,50]

While there is, again, no clear trend related to Hf content, $\rho(T)$ of the Ni-rich samples is generally lower than that of the Ni-stoichiometric ones. The $Ti_{0.9}Hf_{0.1}Ni_1Sn$/$Ti_{0.9}Hf_{0.1}Ni_{1.1}Sn$ sample pair is the notable exception to this observation.

Results of the TE transport measurements do not prove any obvious relation of both $S(T)$ and $\rho(T)$ with their refined microstructural composition, despite the significant spread of investigated compositions and phase relations. This, somewhat disappointing, absence of a simple relationship is, however, as much a result, as the opposite finding would have been. Our study indicates that despite all the microstructural variations and structural features of the investigated samples, the thermoelectric transport in these compounds can still be described by charge carriers populating the regular bulk band structure of the half Heusler system, without exotic scattering mechanisms. In more detail, we can discuss the

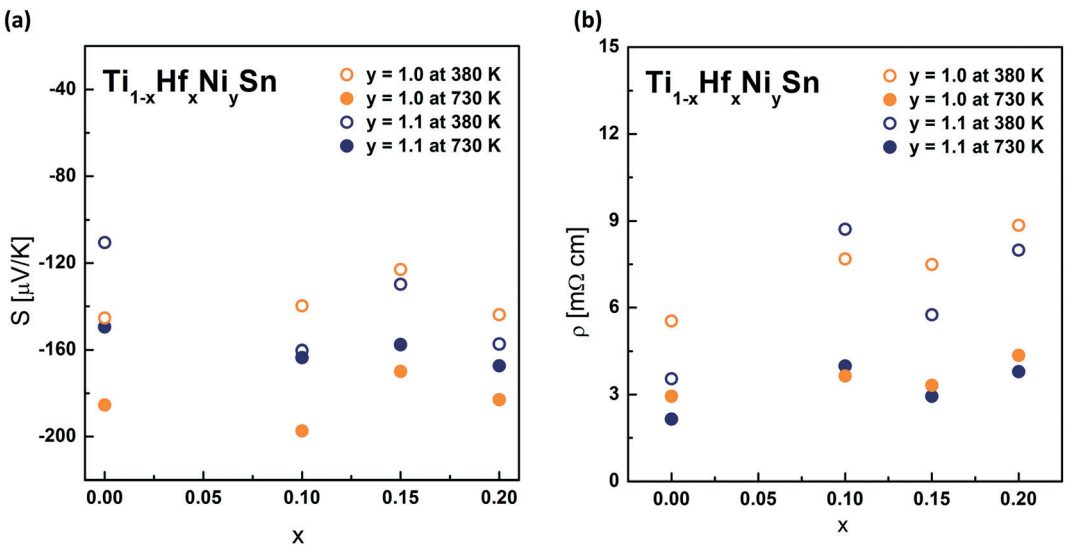

Fig. 9 (a) Composition dependence of the Seebeck coefficient S and (b) electrical resistivity ρ for the $Ti_{1-x}Hf_xNi_ySn$ sample series at 380 and 730 K.

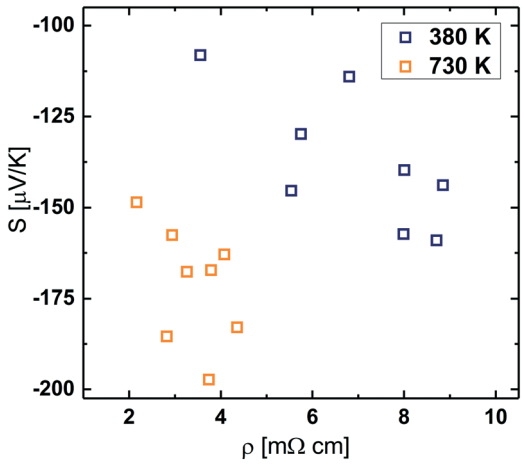

Fig. 10 The Seebeck coefficient (S) plotted against electrical resistivity (ρ) for all $Ti_{1-x}Hf_xNi_{1.0/1.1}Sn$ samples at 380 and 730 K.

observed transport properties in the light of the (micro)structural features of the samples as presented in section high-resolution SR-PXD and TEM. To that end, it is helpful to shortly review different scenarios that have been proposed to explain the promising TE properties of similar half-Heusler compositions. A popular concept of engineering high-performance thermoelectric materials is that of energy filtering, where scattering of electrons at the coherent interfaces between the matrix and nanoprecipitates is assumed to be highly sensitive to the energy of the charge carrier.[9,10,46,51–53] This results in an effective trapping of low energy carriers and thereby increase of $S(T)$ without negatively affecting the electrical resistivity. However, due to the number of influencing parameters, it is difficult to unambiguously confirm this phenomenon experimentally. For half-Heusler systems, interfaces between the HH-matrix and metallic FH-nanoinclusion have been discussed as a potential source of energy filtering.[9] It has also been argued that inclusions of insulating ZrO_2 or HfO_2 have a similar effect.[44–46,51,52,54] It should be noted, however, that while the authors of both works discuss the data in the light of energy filtering, their observations are qualitatively different: Makongo *et al.*[9] report for HH/FH composites an increasing thermopower with a decreasing carrier concentration, while for HH/ZrO_2 composites reported by Chen *et al.*[51] the alleged increase of thermopower was accompanied by an increase in carrier concentration. In the sample series investigated in this work neither the presence of substantial amounts of HfO_2 (also in form of nanoinclusions) nor that of full-Heusler phase leads to a substantial change of the TE transport parameters, as compared to the samples without those additional phases (ESI†). A precipitate induced energy filtering does not seem to play a significant role in the studied sample series. This is in general agreement with earlier work.[12] However, energy filtering requires charge carriers of different energy in order to be effective, *i.e.* fairly high extrinsic doping levels. The samples studied here are nominally undoped, so that a potential energy filtering effect could remain undetected.

Conclusions

The investigated polycrystalline samples of the $Ti_{1-x}Hf_xNi_{1.0/1.1}Sn$ series show the formation of single or multiple Hf-incorporating HH phase(s), of which most contain disorderly distributed Ni at the nominally vacant 4d site. While Hf-based compositions show a tendency to formation of HfO_2 nano-inclusions in the HH matrix, samples containing overstoichiometric Ni crystallize with the micrometer-sized FH phase. Neither occurrence of HfO_2 precipitates nor presence of extra interstitial Ni or HH phase separation appears to influence significantly the electric transport properties of the investigated samples. The interstitial Ni atoms occupying the nominally vacant fcc sublattice (the 4d site) in the HH phase do not tend to crystallize as FH nanoinclusion. Instead, they appear to stay inside the HH crystal structure and form orderly arranged additional plane, absent in the pristine HH compound. The local atomic arrangement resembles closely the Ni atom distribution in the FH phase, but the question whether the observed configuration should be perceived as a defective HH and/or FH crystal structure remains open.

Conflicts of interest

There are no conflicts to declare.

Acknowledgements

This work was funded by the Research Council of Norway within the THELMA (No. 228854) project. The authors acknowledge the skillful assistance of the staff at Swiss-Norwegian (SNBL, BM31) beamline (ESRF, Grenoble, France) and the support of the Norwegian Research Council through the Norwegian Center for Transmission Electron Microscopy (NORTEM).

References

1 L. E. Bell, *Science*, 2008, **321**, 1457–1461.
2 W. G. Zeier, J. Schmitt, G. Hautier, U. Aydemir, Z. M. Gibbs, C. Felser and G. J. Snyder, *Nat. Rev. Mater.*, 2016, **1**, 1–10.
3 T. Graf, C. Felser and S. S. P. Parkin, *Prog. Solid State Chem.*, 2011, **39**, 1–50.
4 R. A. Downie, D. A. MacLaren and J. W. G. Bos, *J. Mater. Chem. A*, 2014, **2**, 6107–6114.
5 S. Chen and Z. F. Ren, *Mater. Today*, 2013, **16**, 387–395.
6 J. W. Bos and R. A. Downie, *J. Phys.: Condens. Matter*, 2014, **26**, 433201.
7 W. J. Xie, A. Weidenkaff, X. F. Tang, Q. J. Zhang, J. Poon and T. M. Tritt, *Nanomaterials*, 2012, **2**, 379–412.
8 M. Schrade, K. Berland, S. N. H. Eliassen, M. N. Guzik, C. Echevarria-Bonet, M. H. Sorby, P. Jenus, B. C. Hauback, R. Tofan, A. E. Gunnaes, C. Persson, O. M. Lovvik and T. G. Finstad, *Sci. Rep.*, 2017, **7**, 13760.
9 J. P. A. Makongo, D. K. Misra, X. Y. Zhou, A. Pant, M. R. Shabetai, X. L. Su, C. Uher, K. L. Stokes and P. F. P. Poudeu, *J. Am. Chem. Soc.*, 2011, **133**, 18843–18852.

10 Y. F. Liu, P. Sahoo, J. P. A. Makongo, X. Y. Zhou, S. J. Kim, H. Chi, C. Uher, X. Q. Pan and P. F. P. Poudeu, *J. Am. Chem. Soc.*, 2013, **135**, 7486–7495.

11 G. Joshi, T. Dahal, S. Chen, H. Z. Wang, J. Shiomi, G. Chen and Z. F. Ren, *Nano Energy*, 2013, **2**, 82–87.

12 C. S. Birkel, J. E. Douglas, B. R. Lettiere, G. Seward, N. Verma, Y. C. Zhang, T. M. Pollock, R. Seshadri and G. D. Stucky, *Phys. Chem. Chem. Phys.*, 2013, **15**, 6990–6997.

13 C. S. Birkel, J. E. Douglas, B. R. Lettiere, G. Seward, Y. C. Zhang, T. M. Pollock, R. Seshadri and G. D. Stucky, *Solid State Sci.*, 2013, **26**, 16–22.

14 J. E. Douglas, C. S. Birkel, M. S. Miao, C. J. Torbet, G. D. Stucky, T. M. Pollock and R. Seshadri, *Appl. Phys. Lett.*, 2012, **101**, 183902.

15 J. E. Douglas, C. S. Birkel, N. Verma, V. M. Miller, M. S. Miao, G. D. Stucky, T. M. Pollock and R. Seshadri, *J. Appl. Phys.*, 2014, **115**, 043720.

16 J. E. Douglas, P. A. Chater, C. M. Brown, T. M. Pollock and R. Seshadri, *J. Appl. Phys.*, 2014, **116**, 163514.

17 R. A. Downie, S. A. Barczak, R. I. Smith and J. W. G. Bos, *J. Mater. Chem. C*, 2015, **3**, 10534–10542.

18 R. A. Downie, D. A. MacLaren, R. I. Smith and J. W. G. Bos, *Chem. Commun.*, 2013, **49**, 4184–4186.

19 R. A. Downie, R. I. Smith, D. A. MacLaren and J. W. G. Bos, *Chem. Mater.*, 2015, **27**, 2449–2459.

20 N. Verma, J. E. Douglas, S. Kramer, T. M. Pollock, R. Seshadri and C. G. Levi, *Metall. Mater. Trans. A*, 2016, **47a**, 4116–4127.

21 Y. W. Chai and Y. Kimura, *Acta Mater.*, 2013, **61**, 6684–6697.

22 T. Katayama, S. W. Kim, Y. Kimura and Y. Mishima, *J. Electron. Mater.*, 2003, **32**, 1160–1165.

23 S. W. Kim, Y. Kimura and Y. Mishima, *Intermetallics*, 2007, **15**, 349–356.

24 M. Gurth, G. Rogl, V. V. Romaka, A. Grytsiv, E. Bauer and P. Rogl, *Acta Mater.*, 2016, **104**, 210–222.

25 K. S. Kim, Y. M. Kim, H. Mun, J. Kim, J. Park, A. Y. Borisevich, K. H. Lee and S. W. Kim, *Adv. Mater.*, 2017, **29**, 1702091.

26 M. Schwall, *PhD Thesis*, Johannes Gutenberg University Mainz, 2012.

27 M. N. Guzik, C. Echevarria-Bonet, M. D. Riktor, P. A. Carvalho, A. E. Gunnæs, M. H. Sørby and B. C. Hauback, *Acta Mater.*, 2018, **148**, 216–224.

28 H. Xie, H. Wang, C. Fu, Y. Liu, G. J. Snyder, X. Zhao and T. Zhu, *Sci. Rep.*, 2014, **4**, 6888.

29 H. H. Xie, J. L. Mi, L. P. Hu, N. Lock, M. Chirstensen, C. G. Fu, B. B. Iversen, X. B. Zhao and T. J. Zhu, *CrystEngComm*, 2012, **14**, 4467–4471.

30 H. Hazama, R. Asahi, M. Matsubara and T. Takeuchi, *J. Electron. Mater.*, 2010, **39**, 1549–1553.

31 H. Hazama, M. Matsubara, R. Asahi and T. Takeuchi, *J. Appl. Phys.*, 2011, **110**, 063710.

32 J. Rodriguez-Carvajal, *Phys. B*, 1993, **192**, 55–69.

33 D. R. G. Mitchell, *Microsc. Res. Tech.*, 2008, **71**, 588–593.

34 M. Schrade, H. Fjeld, T. Norby and T. G. Finstad, *Rev. Sci. Instrum.*, 2014, **85**, 103906.

35 G. Kresse and J. Furthmuller, *Phys. Rev. B: Condens. Matter Mater. Phys.*, 1996, **54**, 11169–11186.

36 J. P. Perdew, K. Burke and M. Ernzerhof, *Phys. Rev. Lett.*, 1996, **77**, 3865–3868.

37 Y. Kimura and Y. W. Chai, *JOM*, 2015, **67**, 233–245.

38 V. V. Romaka, P. Rogl, L. Romaka, Y. Stadnyk, N. Melnychenko, A. Grytsiv, M. Falmbigl and N. Skryabina, *J. Solid State Chem.*, 2013, **197**, 103–112.

39 A. Berche, J. C. Tedenac and P. Jund, *Scr. Mater.*, 2017, **139**, 122–125.

40 Y. Kimura, H. Ueno and Y. Mishima, *J. Electron. Mater.*, 2009, **38**, 934–939.

41 Y. Murayama, S. Sasaki, H. Kimura and A. Chiba, *Mater. Sci. Forum*, 2010, **654–656**, 2114–2117.

42 J. M. Mena, H. G. Schoberth, T. Gruhn and H. Emmerich, *Acta Mater.*, 2016, **111**, 157–165.

43 A. Page, A. Van der Ven, P. F. P. Poudeu and C. Uher, *J. Mater. Chem. A*, 2016, **4**, 13949–13956.

44 A. Visconti, C. Navone, J. Leforestier, N. Mingo and G. Bernard-Granger, *J. Alloys Compd.*, 2017, **709**, 36–41.

45 A. Visconti, G. Bernard-Granger, C. Navone, J. Leforestier and N. Mingo, *Scr. Mater.*, 2016, **123**, 100–104.

46 D. Wu, *PhD Thesis*, Univeristy of Virginia, 2013.

47 Y. W. Chai and Y. Kimura, *Appl. Phys. Lett.*, 2012, **100**, 033114.

48 Y. W. Chai, K. Yoshioka and Y. Kimura, *Scr. Mater.*, 2014, **83**, 13–16.

49 S. Singh, S. R. Barman and D. Pandey, *Journal*, 2015, **230**, 13. Q3

50 Y. L. Tang, X. S. Li, L. H. J. Martin, E. C. Reyes, T. Ivas, C. Leinenbach, S. Anand, M. Peters, G. J. Snyder and C. Battaglia, *Energy Environ. Sci.*, 2018, **11**, 311–320.

51 L. D. Chen, X. Y. Huang, M. Zhou, X. Shi and W. B. Zhang, *J. Appl. Phys.*, 2006, **99**, 064305.

52 S. J. Poon, D. Wu, S. Zhu, W. J. Xie, T. M. Tritt, P. Thomas and R. Venkatasubramanian, *J. Mater. Res.*, 2011, **26**, 2795–2802.

53 K. Berland, X. Song, P. A. Carvalho, C. Persson, T. G. Finstad and O. M. Lovvik, *J. Appl. Phys.*, 2016, **119**, 125103.

54 X. Y. Huang, Z. Xu and L. D. Chen, *J. Inorg. Mater.*, 2004, **19**, 25–30.